Geophysical Journal International

Geophys. J. Int. (2020) **223,** 379–397
Advance Access publication 2020 June 27
GJI Gravity, Geodesy and Tides

doi: 10.1093/gji/ggaa313

Lithospheric stress, strain and displacement changes from GRACE-FO time-variable gravity: case study for Sar-e-Pol Zahab Earthquake 2018

Mehdi Eshagh,[1,2] Farzam Fatolazadeh[3] and Robert Tenzer[4]

[1]*Department of Engineering Science, University West, Trollhättan, Sweden. E-mail: mehdi.eshagh@hv.se*
[2]*Faculty of Geodesy and Geomatics Engineering, K. N. Toosi University of Technology, Tehran, Iran*
[3]*Département de Géomatique Appliquée, Université de Sherbrooke, Sherbrooke, Québec, Canada*
[4]*Department of Land Surveying and Geo-Informatics, Hong Kong Polytechnic University, Hong Kong*

Accepted 2020 June 15. Received 2020 June 15; in original form 2020 January 17

SUMMARY

Temporal variations in the Earth's gravity field can be used for monitoring of lithospheric deformations. The network of continuously operating gravity stations is required for this purpose but a global coverage by such network is currently extremely sparse. Temporal variations in long-wavelength part of the Earth's gravity field have been, however, observed by two satellite missions, namely the Gravity Recovery And Climate Experiment (GRACE) and the GRACE Follow-On (GRACE-FO). These satellite gravity observations can be used to study long-wavelength deformations of the lithosphere. Consequently, considering the lithosphere as a spherical elastic shell and solving the partial differential equation of elasticity for it, the stress, strain and displacement inside the lithosphere can be estimated. The lower boundary of this shell is assumed to be stressed by mantle convection, which has a direct relation to the Earth's gravity field according to Runcorn's theory. Changes in gravity field lead to changes in the sublithospheric stress and the stress propagated throughout the lithosphere. In this study, we develop mathematical models in spherical coordinates for describing the stress propagation from the sublithosphere through the lithosphere. We then organize a system of observation equations for finding a special solution to the boundary-value problem of elasticity in the way that provides a stable solution. In contrast, models presented in previously published studies are ill-posed. Furthermore, we use constants of the solution determined from the boundary stresses to determine the strain and displacements leading to these stresses, while in previous studies only the stress has been considered according to rheological properties of the lithosphere. We demonstrate a practical applicability of this theoretical model to estimate the stress–strain redistribution caused by the Sar-e-Pol Zahab 2018 earthquake in Iran by using the GRACE-FO monthly solutions.

Key words: Geopotential theory; Time variable gravity.

1 INTRODUCTION

Studies of gravity field provide information about the Earth's inner structure and processes. In geophysical studies, the focus is mainly given to a gravimetric determination of density interface, such as modelling of a sediment basin architecture or Moho geometry. Considering geodynamic studies that involve mantle convection and tectonic plate motions, the static gravity field has been used, for instance, to determine stresses at the lithosphere–asthenosphere boundary (LAB) induced by a mantle convection flow. Both types of gravimetric solutions that address either the Earth's inner structure or processes are, however, non-unique because many density configurations inside the Earth can be attributed to just one gravity field solution. To avoid this non-unique problem, different assumptions about the Earth's inner structure have to be adopted depending on a particular study. In geodynamic studies, the lithosphere is often approximated by a solid elastic spherical shell buoyant over a viscous mantle. Mantle convection currents yield stresses at LAB.

A propagation of these stresses through the lithosphere could mathematically be described in terms of gravity field based on solving the boundary-value problem of elasticity (Love 1944). Equivalent definitions could be given for the strain and displacements. When considering

time-variable gravity field, these functional relations can be used to describe the stress–strain redistribution and crustal displacements. Consequently, when focusing on gravity variations occurring within a relatively short time period, these functional models can be applied to describe the stress–strain redistribution and crustal displacements caused by earthquakes.

Low-degree global gravitational models have been used to investigate a global mantle convection pattern and its relationship with a tectonic plate configuration and lithospheric stresses. Kaula (1963) developed a gravimetric method based on minimizing the strain energy, while also incorporating topographic information to estimate minimum stresses in an elastic Earth. McKenzie (1967) studied a mantle-heat flow using gravity anomalies. Marsh & Marsh (1976) compiled a 2-D mantle convection pattern from a global gravitational model. Runcorn (1964, 1967) formulated a functional relation between stress and gravity field based on solving Navier–Stokes' equations for modelling horizontal shear stresses. He then used low-degree spherical harmonics of the Earth's gravity field to deduce a global horizontal stress pattern and found their connection with convergent and divergent sites established by plate tectonic theory. Liu (1977, 1978) applied Runcorn's theory to study convection-generated stresses driving tectonic plates. McNutt (1980) used regional gravity data to interpret stresses within the lithosphere. Fu & Huang (1983) extended Runcorn's theory for the full stress tensor inside the lithosphere. In more recent studies, Eshagh (2014) reformulated Runcorn's theory for gravity gradiometry data; see also studies by Eshagh (2015, 2017), Eshagh & Romeshkani (2015), Eshagh & Tenzer (2017) and Eshagh et al. (2016, 2018).

Phillips & Ivins (1979) argued that Runcorn's theory does not describe realistically the actual global mantle convection pattern because it assumes only a constant viscosity in the mantle. Hager & O'Connell (1981) solved mantle-flow equations by incorporating a plate velocity model, radially variable viscosity as well as both poloidal and toroidal flows in the mantle. Ricard *et al.* (1984) and Richards & Hager (1984) proposed to use a global geoid model as information to constrain a radial viscosity structure for solving Hager and O'Connell's theory. In this way, gravity information is incorporated into a mantle-flow solution. Steinberger *et al.* (2001) applied Hager and O'Connell's theory to investigate a global lithospheric stress pattern induced by a global mantle circulation. Medvedev (2016) inferred a stress pattern within the African tectonic plate based on combining methods for a modelling of thermal isostasy and gravitational potential energy.

In studies summarized above, the static gravity field was used to investigate geodynamic phenomena inside the Earth. Such link is possible because mantle convection principally constitutes a lithospheric composition and its thermal state and governs global plate configuration. Consequently, the mass density structure within the lithosphere reflects a global mantle flow and tectonic plate motions. Examples could be given by a long-wavelength pattern in the Earth's global geoidal geometry that reflects a deep mantle density composition. A medium-to-shorter gravity spectrum, on the other hand, reflects mainly a topographic relief as well as lithospheric density heterogeneities. In the free-air gravity anomaly map, for instance, gravity anomaly highs are typically distributed over orogens, while gravity anomaly lows are detected along oceanic subductions (e.g. Tenzer *et al*. 2009, 2012, 2015; Rathnayake *et al.* 2019).

The Gravity Recovery And Climate Experiment (GRACE, Tapley *et al.* 2005) and the GRACE Follow-On (GRACE-FO, Kornfeld *et al.* 2019) gravity-dedicated satellite missions provide information not only about the static gravity field but importantly also its spatio-temporal variations. GRACE and GRACE-FO monthly gravity solutions are the most common products prepared by different processing centres. A monthly temporal resolution of gravity field could be facilitated to investigate short-period tectonic phenomena, such as crustal deformations or stress–strain redistribution caused by large-magnitude earthquakes. This is particularly relevant in regions without a sufficient coverage by continuous global positioning system (GPS) sites. Note that continuously operating GPS sites provide directly information about horizontal and vertical displacements, while the GPS-derived stress and strain rate fields require additional information about rheological properties of the lithosphere. Obviously, a relatively limited spatio-temporal resolution of the GRACE and GRACE-FO monthly solutions restricts more detailed interpretations of seismic deformations, especially in the absence of GPS data.

An earthquake generates a mass redistribution inside the Earth, causing changes in gravity field. In turn, changes in gravity field could be used to study a mass redistribution due to an earthquake. Using dislocation theory, Sun & Okubo (2004) concluded that—on average—GRACE can detect a mass redistribution caused by earthquakes with a magnitude of 7.5 (at the Richter scale) or greater. Following this idea, deformations in forms of surface displacements due to earthquakes have been investigated. Most of these studies are based on combining GPS data with GRACE monthly gravity solutions to observe the co-seismic crustal vertical dilatation or subsidence (e.g. Tesmer *et al.* 2011; Tanaka *et al.* 2015; Zou *et al.* 2015; Pan *et al.* 2016; Gu *et al.* 2017; Wang *et al.* 2017; Wu *et al.* 2017; He *et al.* 2018; Li *et al.* 2020). Moreover, the effect of post-seismic deformations was investigated by Chen *et al.* (2007), or more recently by Xu *et al.* (2017). All these studies used analytical models or observations to understand tectonic deformations caused by earthquakes, but do not provide any information about changes in stress and strain rates that are useful to better understood the earthquake mechanism.

In this study, the approach applied by Liu (1983) and Fu & Huang (1983) is developed further. The system of equations that they derived for solving the boundary-value problem of elasticity is not well conditioned and stable. Eshagh & Tenzer (2017) and Eshagh (2017) applied a pseudo-inverse approach to solve this problem, yielding an oversmooth solution for the stress field. To address both aforementioned theoretical deficiencies, we reformulated here a mathematical model is such a way that this system of equations becomes regular for all frequencies of the solution. Moreover, in almost all published studies, the static gravity field has only been used for a stress modelling. A determination of the corresponding strain and displacements from the modelled stress field has not been considered, especially for variable models of elasticity parameters. We apply the newly developed models to study changes in the stress, strain and displacement caused by the Sar-e-Pol Zahab earthquake that occurred in west Iran on 2018 November 25. The study begins with a derivation of theoretical models in Section 2, followed by a numerical study in Section 3. Results are presented and discussed in Section 4. The study is concluded in Section 5.

2 THEORY

In this section, we recapitulate basic definitions of the stress, strain and displacement theory. We then solve the spherical elasticity boundary-value problem in order to establish functional relationships between the stress, strain and displacement changes and spatio-temporal variations in gravity field. Thereafter, based on defining the boundary values, we develop a system of equations of which inverse solution is stable unlike those presented in previous studies.

2.1 Displacement vector, strain and stress tensors

Assume that based on geodynamical activities some parts of the lithosphere move from one place to another. This corresponds to a change in coordinates of points before and after movement, known as displacement. At a point this displacement can be described by changes of a position vector before and after movement. Consequently, the displacement can also be described in a vector form. The displacement vector **s** then reads

$$\mathbf{s}(r,\theta,\lambda) = s_z\mathbf{e}_z + s_x\mathbf{e}_x + s_y\mathbf{e}_y, \tag{1a}$$

where s_x, s_y and s_z denote the displacement vector components; and $\mathbf{e}_x$, $\mathbf{e}_y$ and $\mathbf{e}_z$ are the unit vector components. The radial, meridional and prime-vertical components of the displacement vector in eq. (1a) are defined in 3-D spherical coordinates (r,θ,λ), where r denotes a geocentric radius, θ is spherical co-latitude and λ is longitude. The displacement vector components s_x, s_y, s_z and the unit vector components $\mathbf{e}_x$, $\mathbf{e}_y$, $\mathbf{e}_z$ on the right-hand side of eq. (1a) are defined in the Local North-Oriented Frame (LNOF) of Cartesian coordinates with x-, y- and z-axes, respectively, oriented northwards, eastwards and radially upward.

In LNOF, the strain tensor **E** is defined by

$$\mathbf{E} = \begin{bmatrix} \varepsilon_{xx} & \varepsilon_{xy} & \varepsilon_{xz} \\ \varepsilon_{xy} & \varepsilon_{yy} & \varepsilon_{yz} \\ \varepsilon_{xz} & \varepsilon_{yz} & \varepsilon_{zz} \end{bmatrix}, \tag{1b}$$

where ε_{xx}, ε_{yy} and ε_{zz} are the normal strain elements; and ε_{xy}, ε_{xz} and ε_{yz} are the shear strain elements.

The strain tensor elements and the displacement vector components are functionally linked by

$$\varepsilon_{zz} = \frac{\partial s_z}{\partial z}, \tag{1c}$$

$$\varepsilon_{xx} = \frac{1}{r}\left(\frac{\partial s_x}{\partial\theta} + s_z\right), \tag{1d}$$

$$\varepsilon_{yy} = \frac{1}{r\sin\theta}\left(\frac{\partial s_y}{\partial\lambda} + s_z\sin\theta + s_x\cos\theta\right), \tag{1e}$$

$$\varepsilon_{xz} = \frac{1}{2}\left(\frac{1}{r}\frac{\partial s_z}{\partial\theta} - \frac{\partial s_x}{\partial r} + \frac{s_x}{r}\right), \tag{1f}$$

$$\varepsilon_{yz} = \frac{1}{2}\left(\frac{1}{r\sin\theta}\frac{\partial s_z}{\partial\lambda} + \frac{\partial s_y}{\partial r} - \frac{s_y}{r}\right), \tag{1g}$$

$$\varepsilon_{xy} = \frac{1}{2r}\left(\frac{1}{\sin\theta}\frac{\partial s_x}{\partial\lambda} + \frac{\partial s_y}{\partial\theta} - s_y\cot\theta\right). \tag{1h}$$

According to a linear elasticity theory, once the strain tensor is determined from the displacement vector, the stress tensor elements can directly be obtained from the strain tensor elements.

A mathematical relationship between the strain tensor τ_{ij} and the displacement vector **s** reads

$$\tau_{ij} = \tilde{\lambda}\delta_{ij}\nabla\cdot\mathbf{s} + \tilde{\mu}\varepsilon_{ij} \quad \text{where } i,j = x,y \text{ and } z. \tag{2a}$$

The elasticity parameters $\tilde{\lambda}$ and $\tilde{\mu}$ in eq. (2a) describe mechanical properties of material, δ_{ij} is the Kronecker delta and $\nabla\cdot\mathbf{s}$ denotes the divergence of displacement vector **s**.

By analogy with a definition of the strain tensor **E** in eq. (1b), we describe the stress tensor τ in the following matrix form (e.g. Means 1976; Stuewe 2007; Zang & Stephenson 2010; Turcotte & Schubert 2014)

$$\tau = \begin{bmatrix} \tau_{xx} & \tau_{xy} & \tau_{xz} \\ \tau_{xy} & \tau_{yy} & \tau_{yz} \\ \tau_{xz} & \tau_{yz} & \tau_{zz} \end{bmatrix}, \tag{2b}$$

where τ_{xx}, τ_{yy} and τ_{zz} are the normal stress elements; and τ_{xy}, τ_{xz} and τ_{yz} are the shear stress elements.

If $i = j$, the normal stress elements are linked with the normal strain elements as well as with the volumetric strain. Consequently, the divergence of strain must be computed according to a functional model formulated for displacement field. Alternatively, the divergence of strain could be computed numerically. This quantity is needed when normal stresses are desired because the shear stresses are directly related to the shear strain without involvement of the divergence of displacement vector.

Substituting the strain tensor elements from eq. (2a) to the expressions in eqs (1c)–(1h), the stress tensor elements are defined in terms of the strain tensor elements and the displacement vector components. We then write

$$\tau_{zz} = \tilde{\lambda}\,\nabla\cdot\mathbf{s} + 2\tilde{\mu}\frac{\partial s_z}{\partial r}, \tag{2c}$$

$$\tau_{xx} = \tilde{\lambda}\,\nabla\cdot\mathbf{s} + \frac{2\tilde{\mu}}{r}\left(\frac{\partial s_x}{\partial\theta} + s_z\right), \tag{2d}$$

$$\tau_{yy} = \tilde{\lambda}\,\nabla\cdot\mathbf{s} + \frac{2\tilde{\mu}}{r\sin\theta}\left(\frac{\partial s_y}{\partial\lambda} + s_z\sin\theta + s_x\cos\theta\right), \tag{2e}$$

$$\tau_{xz} = \tilde{\mu}\left(\frac{1}{r}\frac{\partial s_z}{\partial\theta} + \frac{\partial s_x}{\partial r} - \frac{s_x}{r}\right), \tag{2f}$$

$$\tau_{yz} = \tilde{\mu}\left(\frac{1}{r\sin\theta}\frac{\partial s_z}{\partial\lambda} + \frac{\partial s_y}{\partial r} - \frac{s_y}{r}\right), \tag{2g}$$

$$\tau_{xy} = \frac{\tilde{\mu}}{r}\left(\frac{1}{\sin\theta}\frac{\partial s_\theta}{\partial\lambda} + \frac{\partial s_\lambda}{\partial\theta} - s_\lambda\cot\theta\right). \tag{2h}$$

We note that mechanical properties of a lithospheric shell are considered through the elasticity parameters $\tilde{\lambda}$ and $\tilde{\mu}$. In most of studies, only constant values have been attributed to these parameters. Nowadays, however, laterally variable values of these parameters can be computed from available seismic models, such as the CRUST1.0 (Laske *et al.* 2013) global crustal seismic model.

2.2 Solution to spherical elasticity boundary-value problem

Let us assume that the lithosphere is a thin elastic shell. The shell displacement can then be described by the following spherical elasticity partial differential equation

$$\left(\tilde{\lambda}+\tilde{\mu}\right)\nabla\left(\nabla\cdot\mathbf{s}\right) + \tilde{\mu}\,\nabla^2\mathbf{s} = 0, \tag{3a}$$

where $\mathbf{s}$ is the displacement vector (see eq. 1a), and ∇^2 denotes the Laplacian operator.

A generalized solution to the spherical elasticity partial differential equation in eq. (3a) has been presented by Love (1944) and later by Fu & Huang (1983) in the following form

$$\mathbf{s} = \sum_{n=0}^{\infty}\left[A\left(r^2\nabla\omega_n + r\alpha_n\omega_n\mathbf{e}_r\right) + B\left(r^2\nabla\bar{\omega}_n + r\bar{\alpha}_n\bar{\omega}_n\mathbf{e}_r\right) + C\nabla\phi_n + D\nabla\bar{\phi}_n\right], \tag{3b}$$

where A, B, C and D are constant coefficients that can be determined from the boundary values. The parameters α_n and $\bar{\alpha}_n$ in eq. (3b) read (cf. Fu & Huang 1983)

$$\alpha_n = -2\frac{n\,\tilde{\lambda} + (3n+1)\,\tilde{\mu}}{(n+3)\,\tilde{\lambda} + (n+5)\,\tilde{\mu}}, \tag{3c}$$

$$\bar{\alpha}_n = 2\frac{(n+1)\,\tilde{\lambda} + (3n+2)\,\tilde{\mu}}{(2-n)\,\tilde{\lambda} + (4-n)\,\tilde{\mu}}, \tag{3d}$$

and ω_n, ϕ_n, $\bar{\omega}_n$ and $\bar{\phi}_n$ are, respectively, the Laplace coefficients of scalar spherical functions ω, ϕ, $\bar{\omega}$ and $\bar{\phi}$.

The Laplace coefficients ω_n, ϕ_n, $\bar{\omega}_n$ and $\bar{\phi}_n$ are related with the Laplace coefficients T_n of the disturbing gravity potential T (i.e. difference between the actual and normal gravity potentials W and U respectively; $T = W - U$) as follows (cf. Fu & Huang 1990)

$$\omega_n = \phi_n = \frac{1}{R}\left(\frac{r}{R}\right)^n T_n \quad r \le R, \tag{3e}$$

$$\bar{\omega}_n = \bar{\phi}_n = \frac{1}{R_1}\left(\frac{R_1}{r}\right)^{n+1} T_n \text{ with } R_1 = (R - D_{\text{Lith}}) \le r, \tag{3f}$$

where r is the geocentric radius of a point inside the lithosphere, D_{Lith} is the lithospheric shell thickness, R is a radius of the upper bound of lithospheric shell and R_1 is a radius of the lower bound of lithospheric shell. The ratio $(r/R)^n$ in eq. (3e) is a damping factor, which attenuates higher frequencies of T_n spectrally from the upper spherical boundary with a radius R to the one with a radius r. Equivalently, $(R_1/r)^n$ reduces higher frequencies from the lower spherical boundary.

Inserting from eqs (3e), (3f) to eq. (3b) and after some algebra, we write the following three identities

$$s_z = \sum_{n=0}^{\infty}\left(A\left(\frac{r}{R}\right)^{n+1}(n+\alpha_n) + B\left(\frac{R_1}{r}\right)^{n}(-(n+1)+\bar{\alpha}_n) + \frac{C}{R^2}\left(\frac{r}{R}\right)^{n-1}n - \frac{D\,(n+1)}{(R_1)^2}\left(\frac{R_1}{r}\right)^{n+2}\right)T_n, \tag{3g}$$

$$s_x = \sum_{n=0}^{\infty}\left(A\left(\frac{r}{R}\right)^{n+1} + B\left(\frac{R_1}{r}\right)^{n} + \frac{C}{R^2}\left(\frac{r}{R}\right)^{n-1} + \frac{D}{(R_1)^2}\left(\frac{R_1}{r}\right)^{n+2}\right)\frac{\partial T_n}{\partial\theta}, \tag{3h}$$

$$s_y = \sum_{n=0}^{\infty}\left(A\left(\frac{r}{R}\right)^{n+1} + B\left(\frac{R_1}{r}\right)^{n} + \frac{C}{R^2}\left(\frac{r}{R}\right)^{n-1} + \frac{D}{(R_1)^2}\left(\frac{R_1}{r}\right)^{n+2}\right)\frac{1}{\sin\theta}\frac{\partial T_n}{\partial\lambda}. \tag{3i}$$

The expressions in eqs (3g)–(3i) define the components s_x, s_y and s_z of the displacement vector $\mathbf{s}$ in terms of the disturbing potential coefficients T_n and their horizontal (meridional and prime-vertical) derivatives $\partial T_n/\partial\theta$ and $\partial T_n/\partial\lambda$.

Note that the spherical harmonic expansions in eqs (3g)–(3i) are defined for $n \geq 0$. Nevertheless, the disturbing potential coefficients T_n typically do not involve the zero- and first-degree terms (meaning that the total mass of the reference ellipsoid equals the total mass of the Earth including the atmosphere, and the origin of the coordinate system is identical to the mass centre of the Earth). In this case, the summation starts from $n = 2$. In studies of mantle convection, long-wavelength spherical harmonics even up to higher degree are often disregarded, as they are mainly attributed to a gravitational contribution from the core and lower mantle.

From eqs (3g)–(3i), the spherical divergence of displacement vector in eq. (3b) becomes

$$\nabla\cdot\mathbf{s} = \sum_{n=0}^{\infty}\left\{A\left[2n+\alpha_n(3+n)\left(\frac{r}{R}\right)^{n+1}\right] + B\left[-2(n+1)+\bar{\alpha}_n(2-n)\left(\frac{R_1}{r}\right)^{n}\right]\right\}\frac{T_n}{r}. \tag{3j}$$

From eqs (1c)–(1h), solutions to individual elements of the strain tensor could be found in the following generalized forms

$$\varepsilon_{zz} = \frac{1}{r}\sum_{n=0}^{\infty}K_n^2 T_n, \tag{4a}$$

$$\varepsilon_{xx} = \frac{1}{r}\sum_{n=0}^{\infty}\left(K_n^3 T_n + K_n^5\frac{\partial^2 T_n}{\partial\theta^2}\right), \tag{4b}$$

$$\varepsilon_{yy} = \frac{1}{r}\sum_{n=0}^{\infty}\left\{K_n^3 T_n + K_n^5\left(\frac{1}{\sin^2\theta}\frac{\partial^2 T_n}{\partial\lambda^2} + \cot\theta\frac{\partial T_n}{\partial\theta}\right)\right\}, \tag{4c}$$

$$\varepsilon_{xz} = \frac{1}{2r}\sum_{n=0}^{\infty}K_n^4\frac{\partial T_n}{\partial\theta}, \tag{4d}$$

$$\varepsilon_{yz} = \frac{\tilde{\mu}}{2r\sin\theta}\sum_{n=0}^{\infty}K_n^4\frac{\partial T_n}{\partial\lambda}, \tag{4e}$$

$$\varepsilon_{xy} = \frac{1}{2r\sin\theta}\sum_{n=0}^{\infty}\left\{K_n^5\left(\frac{\partial^2 T_n}{\partial\theta\partial\lambda} - \cot\theta\frac{\partial T_n}{\partial\lambda}\right)\right\}, \tag{4f}$$

where

$$\begin{aligned} K_n^2 = {} & A(n+\alpha_n)(n+1)\left(\frac{r}{R}\right)^{n+1} \\ & - Bn\left[\bar{\alpha}_n - (n+1)\right]\left(\frac{R_1}{r}\right)^{n} + \frac{C}{R^2}(n-1)n\left(\frac{r}{R}\right)^{n-1} \\ & + \frac{D}{R_1^2}(n+1)(n+2)\left(\frac{R_1}{r}\right)^{n+2}, \end{aligned} \tag{4g}$$

$$K_n^3 = A\,(n+\alpha_n)\left(\frac{r}{R}\right)^{n+1} + B\,[\bar{\alpha}_n - (n+1)]\left(\frac{R_1}{r}\right)^{n} + \frac{C}{R^2}n\left(\frac{r}{R}\right)^{n+1} - \frac{D}{R_1^2}(n+1)\left(\frac{R_1}{r}\right)^{n+2}, \tag{4h}$$

$$K_n^4 = A\left(\frac{r}{R}\right)^{n+1}(2n+\alpha_n) + B\left(\frac{R_1}{r}\right)^{n}(\bar{\alpha}_n - 2\,(n+1)) + \frac{2C}{R^2}\left(\frac{r}{R}\right)^{n-1}(n-1) - \frac{2D}{R_1^2}(n+2)\left(\frac{R_1}{r}\right)^{n+2}, \tag{4i}$$

$$K_n^5 = A\left(\frac{r}{R}\right)^{n+1} + B\left(\frac{R_1}{r}\right)^{n} + \frac{C}{R^2}\left(\frac{r}{R}\right)^{n-1} + \frac{D}{R_1^2}\left(\frac{R_1}{r}\right)^{n+2}. \tag{4j}$$

As evident from the expressions in eqs. (4g)–(4j), the coefficients A and C are related to a signal frequency reduction from the upper boundary of spherical shell, while B and D from the lower boundary. This means that both signal frequency reductions (i.e. from bottom and top boundaries) occur in each strain element. The value of strain then depends on the distance from the upper and lower boundaries.

Combining eqs (4a)–(4f) and eqs (2c)–(2h), the expressions describing the stress tensor elements are introduced by

$$\tau_{zz} = \frac{1}{r}\sum_{n=0}^{\infty}\left(\tilde{\lambda}\,K_n^1 + 2\tilde{\mu}K_n^2\right)T_n, \tag{5a}$$

$$\tau_{xx} = \frac{1}{r}\sum_{n=0}^{\infty}\left\{\left(\tilde{\lambda}\,K_n^1 + 2\tilde{\mu}K_n^3\right)T_n + 2\tilde{\mu}K_n^5\frac{\partial^2 T_n}{\partial\theta^2}\right\}, \tag{5b}$$

$$\tau_{yy} = \frac{1}{r}\sum_{n=0}^{\infty}\left\{\left(\tilde{\lambda}\,K_n^1 + 2\tilde{\mu}K_n^3\right)T_n + 2\tilde{\mu}K_n^5\left[\frac{1}{\sin^2\theta}\frac{\partial^2 T_n}{\partial\lambda^2} + \cot\theta\frac{\partial T_n}{\partial\theta}\right]\right\}, \tag{5c}$$

$$\tau_{xz} = \frac{\tilde{\mu}}{r}\sum_{n=0}^{\infty}K_n^4\frac{\partial T_n}{\partial\theta}, \tag{5d}$$

$$\tau_{yz} = \frac{\tilde{\mu}}{r\sin\theta}\sum_{n=0}^{\infty}K_n^4\frac{\partial T_n}{\partial\lambda}, \tag{5e}$$

$$\tau_{xy} = \frac{\tilde{\mu}}{r\sin\theta}\sum_{n=0}^{\infty}K_n^5\left(\frac{\partial^2 T_n}{\partial\theta\,\partial\lambda} - \cot\theta\frac{\partial T_n}{\partial\lambda}\right). \tag{5f}$$

The parameters K_n^2, K_n^3,K_n^4 and K_n^5 used in eqs (5a)–(5f) are defined in eqs (4g)–(4j). In addition, we also define K_n^1 in the following form

$$K_n^1 = A\,[2n+\alpha_n\,(3+n)]\left(\frac{r}{R}\right)^{n+1} + B\,[-2\,(n+1)+\bar{\alpha}_n\,(2-n)]\left(\frac{R_1}{r}\right)^{n}. \tag{5g}$$

In definitions of the stress elements in eq. (2a), the diagonal elements involve the volumetric strain (or the divergence of displacement field) and the elasticity parameter $\tilde{\lambda}$. Consequently, it could be expected that values of diagonal elements of the stress tensor are larger than the shear stress (off-diagonal) elements. Nevertheless, we consider that the stress values are limited by the upper and lower boundary values, defined next.

2.3 Boundary values

Generalized solutions to the displacement vector and to the strain and stress tensors (given in Section 2.2) depend on the coefficients A, B, C and D. Their determination requires adopting certain boundary conditions. In our theoretical model, we assume that the radial, northward and eastward forces F_z, F_x and F_y acting at the topographic surface (approximated by the upper bound of lithospheric shell) are zero (cf. Fu & Huang 1983). Hence, we write

$$F_z = 0, \quad F_x = 0, \quad F_y = 0 \qquad \text{for} \quad r = R. \tag{6a}$$

This assumption is justified if we consider the stress due to mantle convection. In this case, the maximum stress occurs at LAB, attenuates upward with an increasing distance from LAB, and vanishes at the surface.

We further consider that the radial force is zero, while only the shear stress is acting at LAB (approximated by the lower bound of lithospheric shell). We then write

$$F_z = 0, \quad F_x = \tau_{xz}, \quad F_y = \tau_{yz} \quad \text{for} \quad r = R - D_{\text{Lith}}. \tag{6b}$$

By assuming that mantle convection drives the lithosphere, the assumption in eq. (6b) is not far from reality, as the shear stress between the mantle and the lithosphere is a driving force. Here, we also assume that mantle convection does not generate a radial force. It is worth mentioning, however, that the stress due to topographic loads can also be considered for a radial force at the lower boundary of spherical shell. In this study, we only focus on spatio-temporal variations in the stress, strain and displacement. Therefore, such force remains constant at least during a relatively short time period. This justifies that a radial force is disregarded. We then write

$$\tau_{zz}\,|_R = \frac{1}{R}\sum_{n=0}^{\infty}\left(\tilde{\lambda}\,K_n^1\,|_R + 2\tilde{\mu}K_n^2\,|_R\right)T_n = \frac{1}{R_1}\sum_{n=0}^{\infty}\left(\tilde{\lambda}K_n^1\,\big|_{R_1} + 2\tilde{\mu}K_n^2\,\big|_{R_1}\right)T_n = 0. \tag{6c}$$

Consequently, we have

$$\tilde{\lambda}\,K_n^1\,|_R + 2\tilde{\mu}K_n^2\,|_R = AH_{1,n} + BH_{2,n}\left(\frac{R_1}{R}\right)^n + \frac{C}{R^2}H_{3,n} + \frac{D}{R_1^2}H_{4,n}\left(\frac{R_1}{R}\right)^{n+2} = 0, \tag{6d}$$

$$\tilde{\lambda}\,K_n^1\,\big|_{R_1} + 2\tilde{\mu}K_n^2\,\big|_{R_1} = AH_{1,n}\left(\frac{R_1}{R}\right)^{n+1} + BH_{2,n} + \frac{C}{R^2}H_{3,n}\left(\frac{R_1}{R}\right)^{n-1} + \frac{D}{R_1^2}H_{4,n} = 0, \tag{6e}$$

where

$$H_{1,n} = \tilde{\mu}\,n\,(2n+\alpha_n) + \left\{2n\left(\tilde{\lambda}+\tilde{\mu}\right) + \alpha_n\left[(n+3)\,\tilde{\lambda} + (n+2)\,\tilde{\mu}\right]\right\}, \tag{6f}$$

$$H_{2,n} = \left[\tilde{\lambda}\,\left(-2\,(n+1) + \bar{\alpha}_n\,(2-n)\right) - 2\tilde{\mu}n\,[\bar{\alpha}_n - (n+1)]\right], \tag{6g}$$

$$H_{3,n} = 2\tilde{\mu}\,\,(n-1)\,n, \tag{6h}$$

$$H_{4,n} = 2\tilde{\mu}\,\,(n+1)\,(n+2)\,. \tag{6i}$$

In eqs (6d) and (6e), we introduced two linear equations from boundary values, but two more are needed to find values for the all four coefficients A, B, C and D. For this, we consider the existence of shear stress at both boundaries.

For the topographic surface, we have

$$\tau_{xz}\,|_R = \sum_{n=0}^{\infty}\left\{\tilde{\mu}\,K_n^4\,|_R\,\frac{\partial T_n}{r\,\partial\theta}\right\} = 0. \tag{7a}$$

From eq. (7a), the third equation is found in the following form

$$K_n^4\,|_R = AG_{1,n} + BG_{2,n}\left(\frac{R_1}{R}\right)^n + \frac{C}{R^2}G_{3,n} + \frac{D}{R_1^2}G_{4,n}\left(\frac{R_1}{R}\right)^{n+1}, \tag{7b}$$

where

$$G_{1,n} = \tilde{\mu}\,\,(2n+\alpha_n)\,, \tag{7c}$$

$$G_{2,n} = \tilde{\mu}\,\,(-2\,(n+1) + \bar{\alpha}_n)\,, \tag{7d}$$

$$G_{3,n} = 2\tilde{\mu}\,\,(n-1)\,, \tag{7e}$$

$$G_{4,n} = -2\tilde{\mu}\,\,(n+2)\,. \tag{7f}$$

For LAB, we adopt Runcorn's definition of the shear stress induced by a mantle convection flow. The northward shear stress element is then considered, but it could be demonstrated that the consequence is the same if the eastward shear stress is applied as well. Setting the

northward shear stress element at LAB (eq. 5d) equal to the northward shear stress presented by Runcorn (1967), we get

$$\tau_{xz}\,|_{R_1} = \tilde{\mu}\sum_{n=0}^{\infty} K_n^4 \frac{\partial T_n}{r\partial\theta}\,|_{R_1} = \frac{g}{4\pi G\,(R-D_{\mathrm{Lith}})}\sum_{n=0}^{\infty}\frac{2n+1}{n+1}\left(\frac{R}{R_1}\right)^{-(n+1)}\frac{\partial T_n}{\partial\theta}, \tag{8a}$$

where G denotes the Newtonian's gravitational constant, and g is gravity.

From eq. (8a), we get

$$K_n^4\,|_{R_1} = A\left(\frac{R_1}{R}\right)^{n+1} G_{1,n} + BG_{2,n} + \frac{C}{R^2}\left(\frac{R_1}{R}\right)^{n-1} G_{3,n} + \frac{D}{R_1^2}G_{4,n}. \tag{8b}$$

The expressions in eqs (6d), (6e), (7b) and (8b) are now used to establish the system of observation equations for finding the parameters A, B, C and D.

The system of observation equations is written in the following vector-matrix form

$$\mathbf{A}_n\mathbf{x}_n = \mathbf{l}_n, \tag{9a}$$

where the design matrix $\mathbf{A}_n$, the vector of observations $\mathbf{l}_{n,}$ and the vector of unknown parameters $\mathbf{x}_n$ read

$$\mathbf{A}_n = \begin{bmatrix} H_{1,n} & H_{2,n}\left(\frac{R_1}{R}\right)^n & H_{3,n} & H_{4,n}\left(\frac{R_1}{R}\right)^{n+2} \\ H_{1,n}\left(\frac{R_1}{R}\right)^{n+1} & H_{2,n} & H_{3,n}\left(\frac{R_1}{R}\right)^{n-1} & H_{4,n} \\ G_{1,n} & G_{2,n}\left(\frac{R_1}{R}\right)^n & G_{3,n} & G_{4,n}\left(\frac{R_1}{R}\right)^{n+2} \\ G_{1,n}\left(\frac{R_1}{R}\right)^{n+1} & G_{2,n} & G_{3,n}\left(\frac{R_1}{R}\right)^{n-1} & G_{4,n} \end{bmatrix},$$

$$\mathbf{l}_n = \begin{bmatrix} 0 \\ 0 \\ 0 \\ F_n \end{bmatrix}, \qquad \mathbf{x}_n = \begin{bmatrix} A \\ B \\ C' \\ D' \end{bmatrix}. \tag{9b}$$

Moreover, we define F_n, C' and D' as follows

$$F_n = \frac{rg}{4\pi G R_1}\frac{2n+1}{n+1}\left(\frac{R}{R_1}\right)^{n+1}, \quad C' = \frac{C}{R^2}, \quad D' = \frac{D}{R_1^2}.. \tag{9c}$$

The solution to find the parameters A, B, C and D in the vector $\mathbf{x}$ reads

$$\mathbf{x}_n = \mathbf{A}_n^{-1}\mathbf{l}_n, \tag{9d}$$

where $\mathbf{A}_n^{-1}$ is the regular inverse of $\mathbf{A}_n$.

It is worth emphasizing here that the matrix $\mathbf{A}_n$ is regular and the system of equations in eq. (9a) is stable, unlike those presented in former studies. Eshagh (2017) and Eshagh & Tenzer (2017) solved this problem by applying a pseudo-inverse in order to find the parameters A, B, C and D but, as mentioned above, the final solution is too smooth. The solution presented in this study mitigate both these problems.

3 NUMERICAL STUDY

Here, we demonstrate an applicability of theoretical models (derived in Section 2) in seismic studies. The methodology is explained on a numerical example that involves modelling of displacement, strain and stress changes caused by the earthquake occurring in 2018 November 25 with the magnitude of 6.3. The earthquake epicentre (34.361° N, 45.744° E) was located near the town Sarpol-e-Zahab in West Iran close to the border with Iraq. We situated our study area between geographical latitudes 15° and 50° N and longitudes 30° and 75° E. Tectonic configuration of the study area and input data acquisition are briefly reviewed next.

3.1 Tectonic setting

From a global tectonic point of view, Iran is part of the Alpine-Himalayan orogenic belt, formed by a collision and convergence of the African, Arabian and Indian plates with Eurasia that caused major crustal shortening and thickening along the Iranian-Himalayan active fold-thrust mountain belt (cf. Stöcklin 1968; Zamani & Hashemi 2004; Zamani *et al.* 2013). It resulted in a formation of the Iranian plateau that is an extensive area of intraplate tectonic deformations trapped between the rigid, old Arabian and Turan Cratons. The most pronounced tectonic feature in Iran is the Zagros Fold and Thrust Belt. It covers most of the western part of Iran, and consists of two major segments divided by the Kazeroun Fault Zone (Alavi 2004; Kaviani *et al.* 2009; Zamani *et al.* 2013). The Alborz Mountain Range separates the South Caspian Sea Basin from the central Iran (Zamani & Hashemi 2000; Zamani & Agh-Atabai 2009), while extending north towards the Kopeh Dagh Mountain Belt that separates central Iran from the Turan Platform (Zamani *et al.* 2008).

The Iranian plateau is recognized as one of the most seismically active area in the world. It has experienced several major and destructive earthquakes in the recent past. Berberian (1976) has divided Iran into four major seismo-tectonics zones, namely the Zagros Fold and Thrust

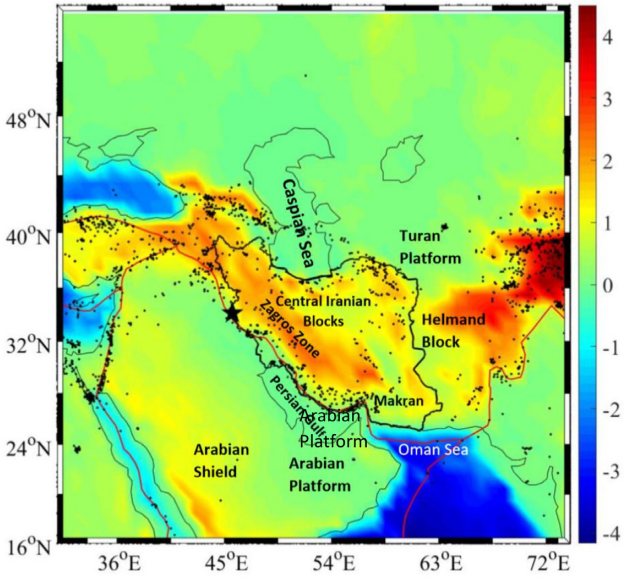

Figure 1. Tectonic setting of the study area superimposed on the solid topography. Tectonic margins between the Arabian and Eurasian plates are indicated by a thick red line. Thin red lines indicate a more detailed tectonic configuration within Iran including its geological provinces according to Pollastro *et al.* (1997). Black dots indicate selected locations of earthquakes occurred up to 2016 (Heidbach *et al.* 2018). Black star indicates a location of the Sar-e-Pol Zahab earthquake (on 2018 November 25).

Belt, Central Iran, Alborz and Koppeh Dagh (Fig. 1). The Alpine-Himalayan belt in Iran is defined by a broad band of diffused seismicity and contains several mobile belts surrounding small, relatively stable blocks. Major zones of mobility in decreasing order of activity are Zagros, Alborz, East Central Iran and the Caucasus and Eastern Turkey, although some small aseismic blocks in central Iran, Azerbaijan and the south Caspian Sea exhibiting noticeable stability have also been identified. A distribution of epicentres indicates that seismicity of the Zagros Fold and Thrust Belt (Fig. 1) is very high, characterized by a large number of shocks in the magnitude ranging from 5 to 6 and a small number of shocks with the magnitude 7 or higher. Central Iran has scattered seismic activity with large magnitude earthquakes. Earthquakes in Central Iran are generally shallow (<70 km) with a few intermediate (70–300 km) earthquakes. A seismic pattern in the Alborz region is discontinuous but with gaps filled in gradually by relatively large events. Most of strong earthquakes occurred in eastern and central Alborz. Earthquakes in Alborz Mountains are mostly shallow or intermediate. Koppeh Dagh is seismically active and the shocks have a shallow focus (Berberian 1976). The southern limit of this activity is not well defined and extends south to the Alborz and Central Iran.

3.2 Data acquisition

3.2.1 Input data and models

We used global topographic and bathymetric data sets from SRTM30 (Farr *et al.* 2007) to generate the coefficients of solid topography with a spectral resolution up to degree of 180. We then used these coefficients to generate a smooth solid topography within the study area with the same spectral resolution (up to degree 180). As seen from regional tectonic plate configuration (see Fig. 1), the earthquake occurred at the convergent tectonic margin separating the Arabian plate from the Iranian block. We used the lithospheric thickness model from Conrad & Lithgow-Bertelloni (2006) to define LAB (Fig. 2a). We see a significant regional lithospheric deepening to about 250 km beneath the Persian Gulf and surrounding parts of the Arabian plate (central part of the Arabian Platform) and the Iranian block. Elsewhere beneath these two tectonic blocks, the lithospheric thickness is roughly 100 km.

The stresses inside the lithosphere depend on mechanical properties of the lithosphere that are defined by the elasticity parameters $\tilde{\mu}$ and $\tilde{\lambda}$. We derived these two parameters from seismic velocities and uppermost mantle densities taken from the CRUST1.0 (Laske *et al.* 2013) global seismic crustal model (using the Matlab code provided by Dr Michael Bevis https://igppweb.ucsd.edu/~gabi/crust1.html; see MATLAB section). Since the density and velocity of seismic waves are given in the CRUST1.0 model, it is rather straightforward to compute the elasticity parameters $\tilde{\mu}$ and $\tilde{\lambda}$from them. The elastic coefficients $\tilde{\mu}$ and $\tilde{\lambda}$ are shown in Figs 2(b) and (c), respectively. Both coefficients have a very similar spatial pattern, with maxima of both coefficients detected within the lithosphere of the Turan Platform. A regional anomaly of relatively large values of both these parameters is also seen beneath the Persian Gulf and the central Arabian Platform. These maxima coincide with regional maxima of the lithospheric elastic thickness (cf. Eshagh *et al.* 2019), confirming a high strength of the Turan and Arabian Platform.

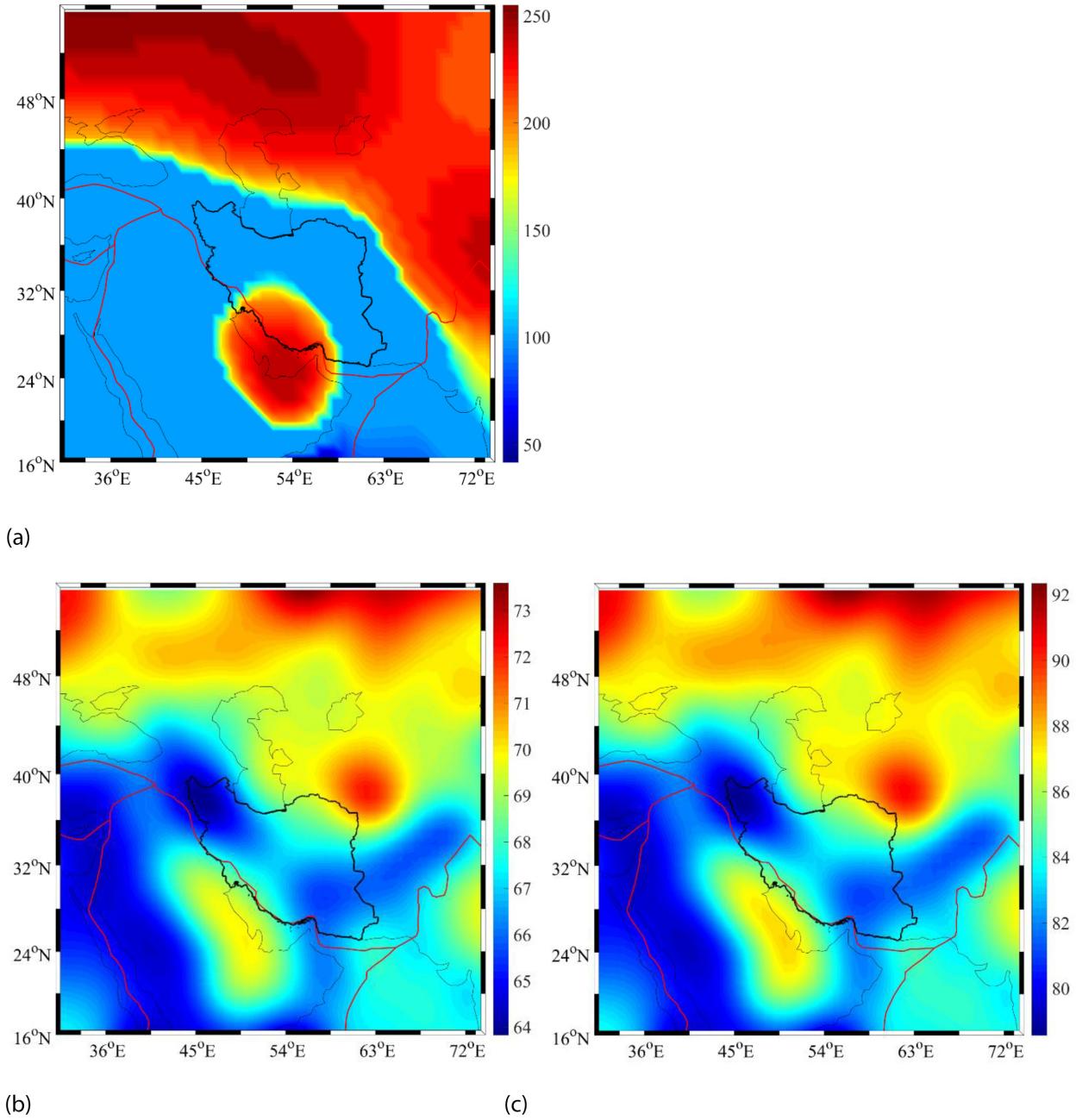

Figure 2. Regional maps of: (a) the lithospheric thickness (km), (b) the elastic coefficient $\tilde{\mu}$ and (c) the elastic coefficient $\tilde{\lambda}$.

3.2.2 Hydrological signal

In order to use the GRACE-FO monthly solutions to investigate a response of the lithosphere to an earthquake, the hydrological signal has to be removed from a time-variable gravity field. For this purpose, we used the newest version of the land surface model (NOAH V2.1) related to the Global Land Data Assimilation System (GLDAS, Rodell *et al.* 2004) to compute gravitational contributions of soil moisture, snow water equivalent and canopies. This model provides information from 2000 to present. It is available at (https://hydro1.gesdisc.eosdis.nasa.gov/data/GLDAS/GLDAS_NOAH10_M.2.1/). It should be noted that the GLDAS model does not provide any information about groundwater and inland waters including lakes, wetlands, rivers and man-made reservoirs. However, we computed these components using other hydrological models and observed that variations of these components are negligible within our study area.

We removed contributions of the three aforementioned components from the GRACE-FO monthly solutions. This computation was realized according to expressions given, for instance, by Wahr *et al.* (1998). Results of a hydrological signal modelling are shown in Fig. 3. We note that our intention is to show the absolute value of these effects in the month before earthquake and then to observe how these components changed after the earthquake. For this purpose, we presented results for the 2018 October and then shown their differences between 2018 December and October. In Fig. 3(a), we plotted the gravitational contribution of hydrological signal in terms of equivalent water heights for

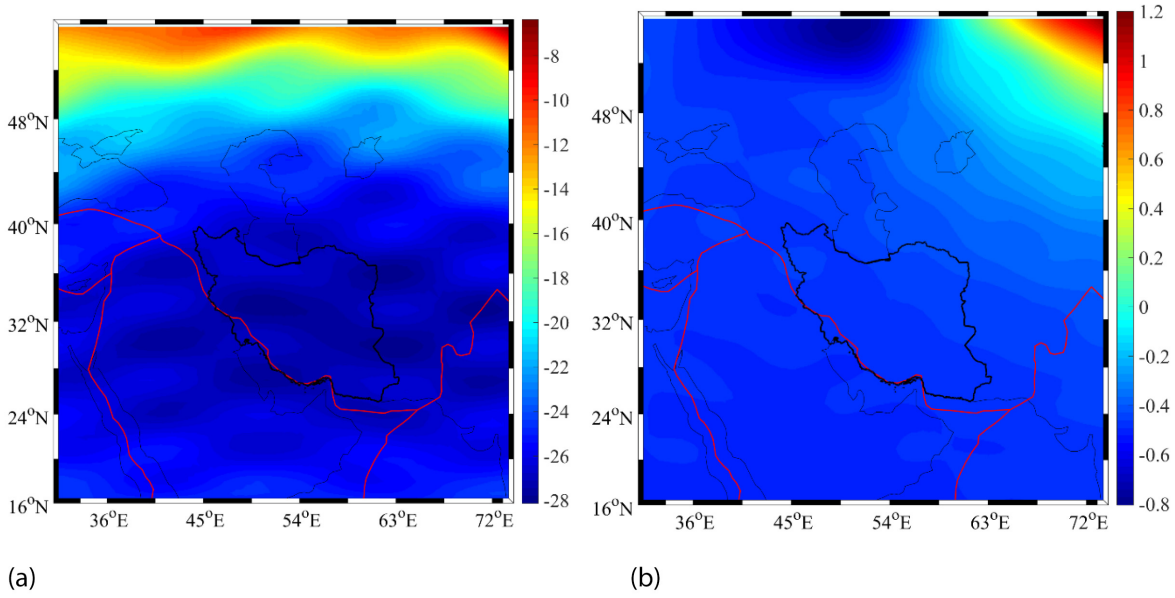

Figure 3. Regional maps of: (a) the gravitational contribution of hydrological signal (in terms of the equivalent water height [mm]) in 2018 October, and (b) its differences (mm) in months after (2018 December) and before (2018 October) the earthquake.

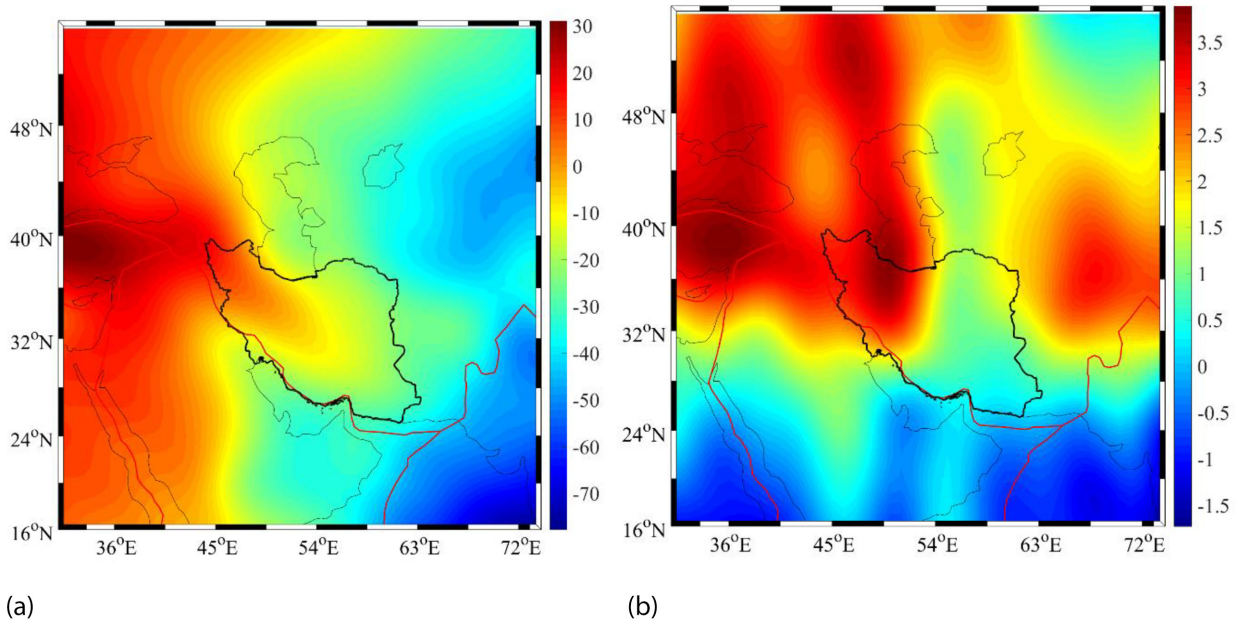

Figure 4. Regional maps of: (a) the GRACE-FO geoid solution (m) for 2018 October, and (b) the geoidal height differences (mm) between the GRACE-FO monthly solutions for 2018 December and October.

the month (2018 October) before the earthquake. In Fig. 3(b), we plotted differences between this gravitational contribution for months after (2018 December) and before (2018 October) the earthquake. Despite the hydrological signal is relatively large (Fig. 2a), exceeding even 20 mm (in absolute sense) in the vicinity of the epicentre, corresponding changes before and after the earthquake are rather small. Within the whole study area these differences are mostly $\pm$ 1 mm.

3.2.3 GRACE-FO model and its changes

The GRACE-FO monthly solutions are provided by sets of spherical harmonics complete up to degree 60. Temporal monthly models provided by the Centre for Space Research (CSR) have been extracted. These data sets are available at: (ftp://icgem.gfz-potsdam.de/01_GRACE/CSR/CSR%20Release%2006%20(GFO)/unfiltered/). Filtering and localization of these coefficients were done based on the method explained in Fatolazadeh *et al.* (2017). We used the GRACE-FO monthly solutions for 2018 October and December. In Fig. 4(a), we plotted the GRACE-FO geoid solution for 2018 October. In Fig. 4(b), we plotted the geoidal height differences between the GRACE-FO monthly solutions for 2018

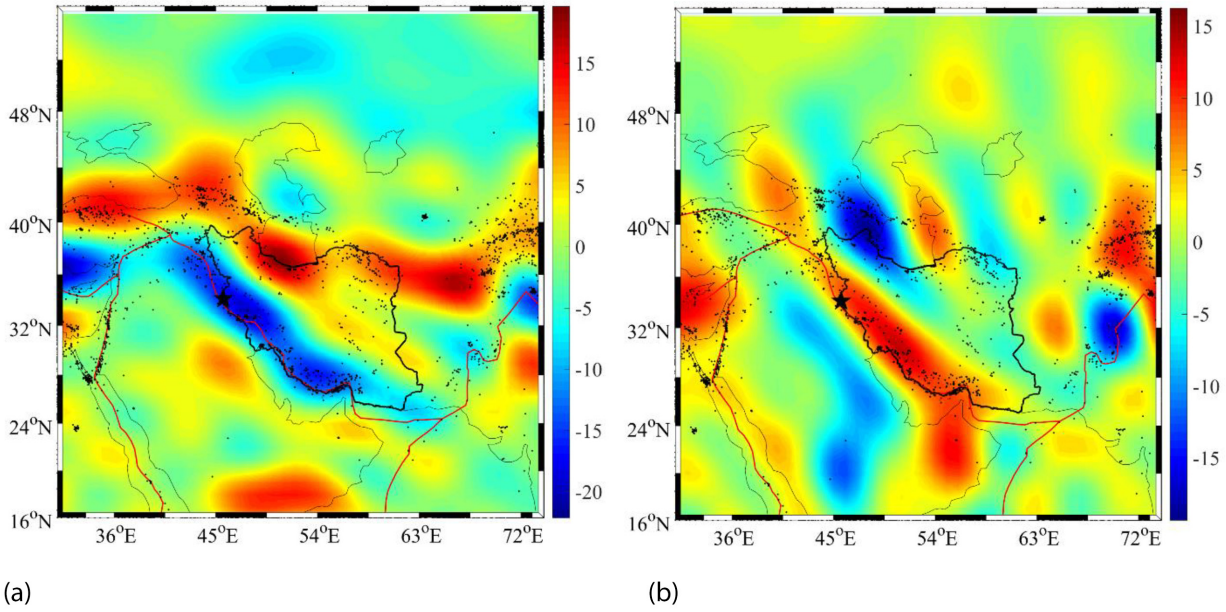

Figure 5. Lithospheric shear stress components: (a) τ_{xz} and (b) τ_{yz} (MPa) computed at LAB using the GRACE-FO monthly solution (from degree 10 to 60) for 2018 October.

December and October. Within the Iranian block, we see maximum changes in geoid heights between these two monthly solutions to about 3.5 mm in the northwest part.

4 RESULTS

Input data and models presented in Section 3 were used to compute the displacement, stress and strain changes. Results are presented next.

4.1 Sublithospheric shear stresses

As explained above, coefficients describing generalized solutions to the displacement, strain and stress are derived from boundary values. At LAB, we considered only the shear stress induced by a mantle convection flow and computed it according to formulae derived by Runcorn (1967). We used the GRACE-FO monthly solution (from degree 10 to 60) for 2018 October corrected for the GLDAS hydrological signal to compute the shear stress at LAB. The LAB depth was computed from topographic heights and bathymetric depths and the lithospheric thickness (Fig. 2a). The stress components τ_{xz} and τ_{yz} computed at LAB are shown in Fig. 5.

We note that the long-wavelength contribution (below degree 10) does not significantly affects the shear stress at LAB because it mostly reflects the Earth's deep structure within the core and lower mantle. Furthermore, the main objection to Runcorn's theory is the dependence of the long-wavelength portion of gravity field on a mantle viscosity structure. Liu (1970), for instance, used degrees between 13 and 25 for this computation by applying Runcorn's theory to address this issue. Similarly, Stewart & Watts (1997) removed degrees below 15 in their computations to estimate the lithospheric elastic thickness. More recently, Bowin (2000) demonstrated that low-degree spherical harmonics below degree 10 represent mostly the contribution from beneath the lithosphere. Therefore, the contribution of mantle radial viscosity structure is reduced by removing low-degree spherical harmonics from the GRACE-FO monthly solutions.

As seen in Fig. 5(a), the northward shear stress component τ_{xz} reaches large negative values (meaning that the shear stress vector component τ_{xz} has a southern orientation) along the active convergent tectonic margin between the Arabian plate and the Iranian block. Elsewhere, this shear stress component is typically positive. As seen in Fig. 5(b), the eastward shear stress component τ_{yz} along the active convergent tectonic margin between the Arabian plate and the Iranian block reaches large positive values (meaning in this case that the shear stress vector component τ_{yz} has a eastward orientation). A prevailing southeast orientation of the shear stress vector is generally parallel to the orientation of this active convergent margin.

4.2 Lithospheric stress tensor

We used the lithospheric shear stress components (shown in Fig. 5) and the elasticity parameters $\tilde{\mu}$ and $\tilde{\lambda}$ (shown in Figs 2b and c) to compute the stress tensor elements at a constant depth of 18 km that is equivalent to depth of the Sar-e-Pol Zahab earthquake hypocentre. The stress tensor elements are shown in Fig. 6. As seen in Fig. 6(a), the stress tensor element τ_{xx} reaches negative values within the Arabian Platform

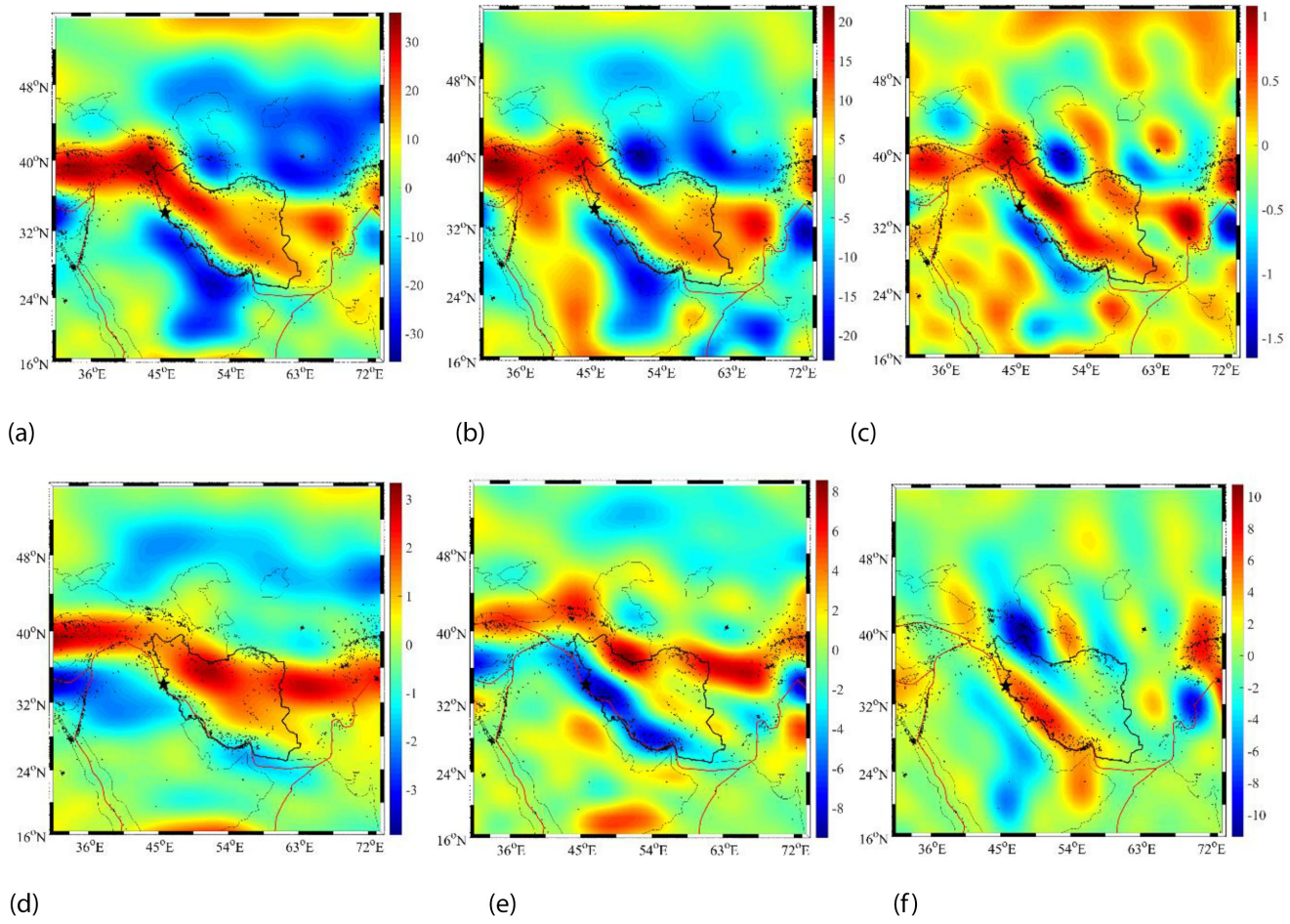

Figure 6. Stress tensor elements: (a) $\tau_{xx,}$ (b) $\tau_{yy,}$ (c) $\tau_{zz,}$ (d) $\tau_{xz,}$ (e) τ_{yz} and (f) τ_{xy} (MPa) computed from the GRACE-FO monthly solution (from degree 10 to 60) for 2018 October.

characterized by a significant lithospheric strength (cf. Chen *et al.* 2015; Eshagh *et al.* 2019). Large negative values are also detected beneath the Caspian Sea Basin that is underlain by a rigid lithospheric block as well as within a stable and rigid lithosphere of the Turan Platform. Positive values apply along the Zagros Fold and Thrust Belt (and other orogenic formations) characterized by a low lithospheric strength. The stress tensor element τ_{yy} has a very similar spatial pattern (Fig. 6b). Values of the stress tensor element τ_{zz} (Fig. 6c) are considerably smaller than the corresponding values of τ_{xx} and τ_{yy}. This finding is not surprising because we assumed that the radial stress at LAB equals zero. The shear stress tensor elements $\tau_{xz,}$ $\tau_{yz,}$ τ_{xy} (Figs 6d–f) reflect the normal stress pattern.

4.3 Lithospheric strain tensor

The strain tensor elements computed from the GRACE-FO monthly solution (from degree 10 to 60) for 2018 October are shown in Fig. 7.

Spatial patterns of the shear strain tensor elements of ε_{xy}, ε_{xz} and ε_{yz} are similar to spatial patterns of the shear stress tensor elements τ_{xy}, τ_{xz} and τ_{yz}. On the other hand, spatial patterns of ε_{xx}, ε_{yy} and ε_{zz} differ from spatial patterns of τ_{xx}, τ_{yy} and τ_{zz}. This is explained by involving of the volumetric strain in the computation of the normal stress elements.

4.4 Displacement vector

The displacement vector components computed from the GRACE-FO monthly solution (from degree 10 to 60) for 2018 October are shown in Fig. 8. Along active tectonic margin between the Arabian plate and the Iranian block we see prevailing eastward displacements in the map of the component s_x (Fig. 8a). We note that positive values of this component indicate eastward deformations, while negative values westward deformations. As seen in Fig. 8(b) for the component $s_{y,}$ southward deformations prevail along this active tectonic margin. Nevertheless, we see also some small northward deformations along this margin in northwest Iran. A spatial pattern of the displacement vector component s_z reveals a prevailing uplift along the Zagros and Kopeh Dagh Fold and Thrust Belts, while the Arabian and Turan Platforms are characterized by a subsidence.

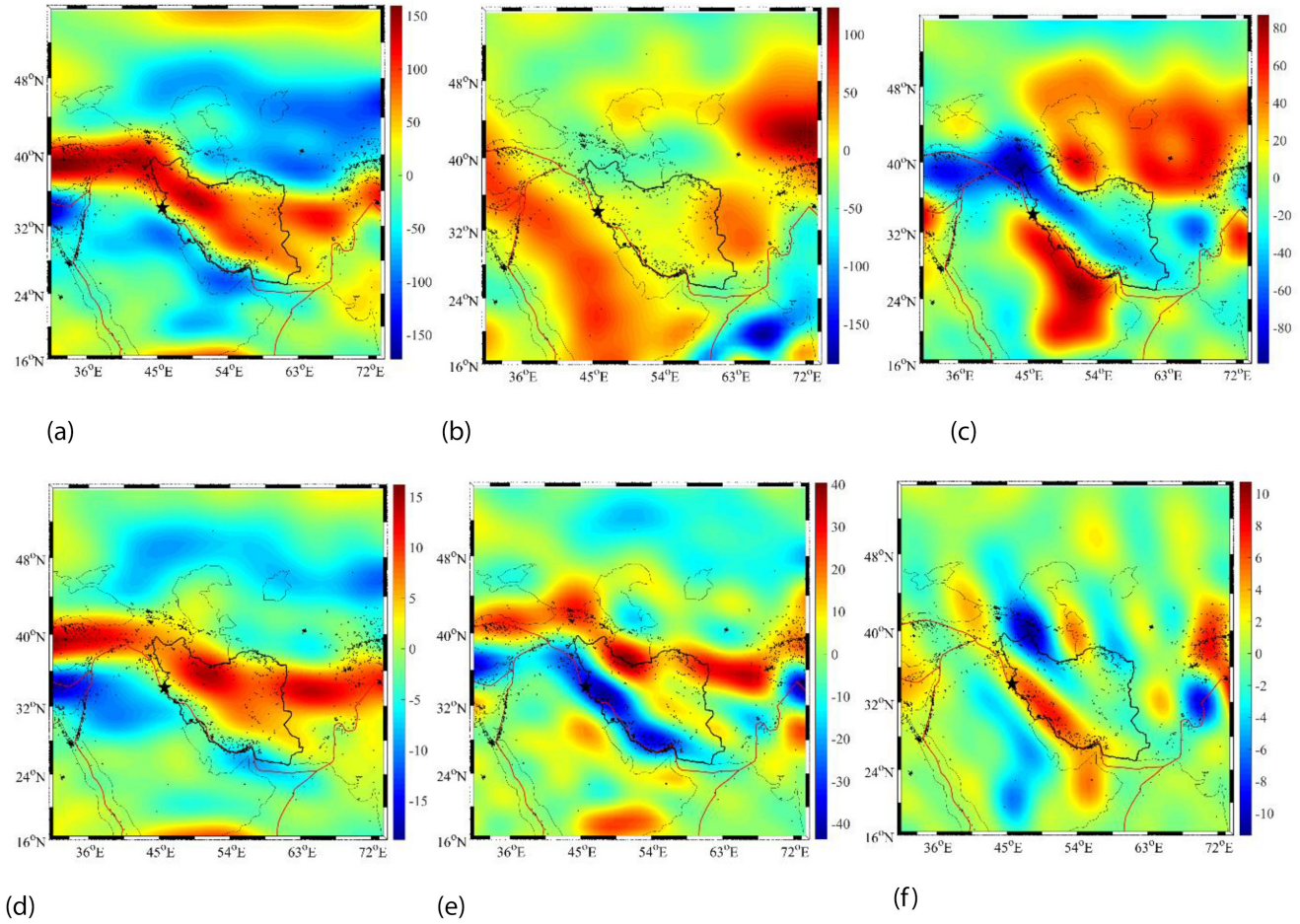

Figure 7. Strain tensor elements: (a) ε_{xx}, (b) ε_{yy}, (c) ε_{zz}, (d) ε_{xz}, (e) ε_{yz} and (f) ε_{xy} computed from the GRACE-FO monthly solution (from degree 10 to 60) for 2018 October.

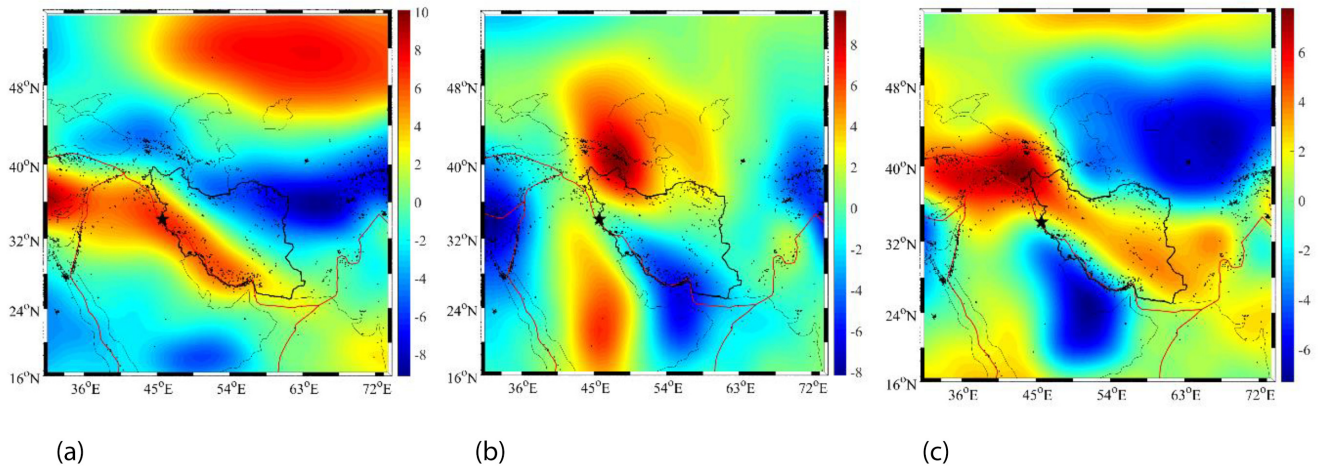

Figure 8. Displacement vector components: (a) s_x, (b) s_y and (c) s_z (mm) computed from the GRACE-FO monthly solution (from degree 10 to 60) for 2018 October.

4.5 Shear stress changes

Changes in the shear stress components τ_{xz} and τ_{yz} at LAB between 2018 December and October are plotted in Fig. 9. As seen in Fig. 9(a), the earthquake trigged only very minor changes in the horizontal shear stress components within the Arabian plate and the Iranian block.

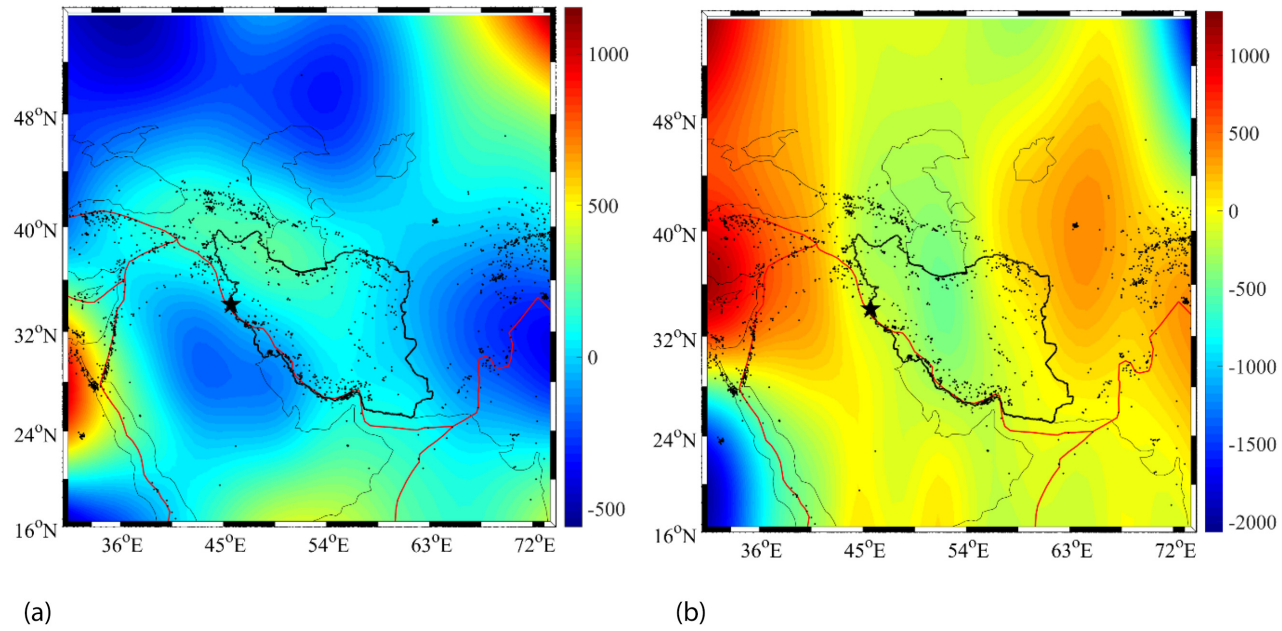

Figure 9. Changes in the shear stress components: (a) τ_{xz} and (b) τ_{yz} (Pa) computed at LAB between 2018 December and October.

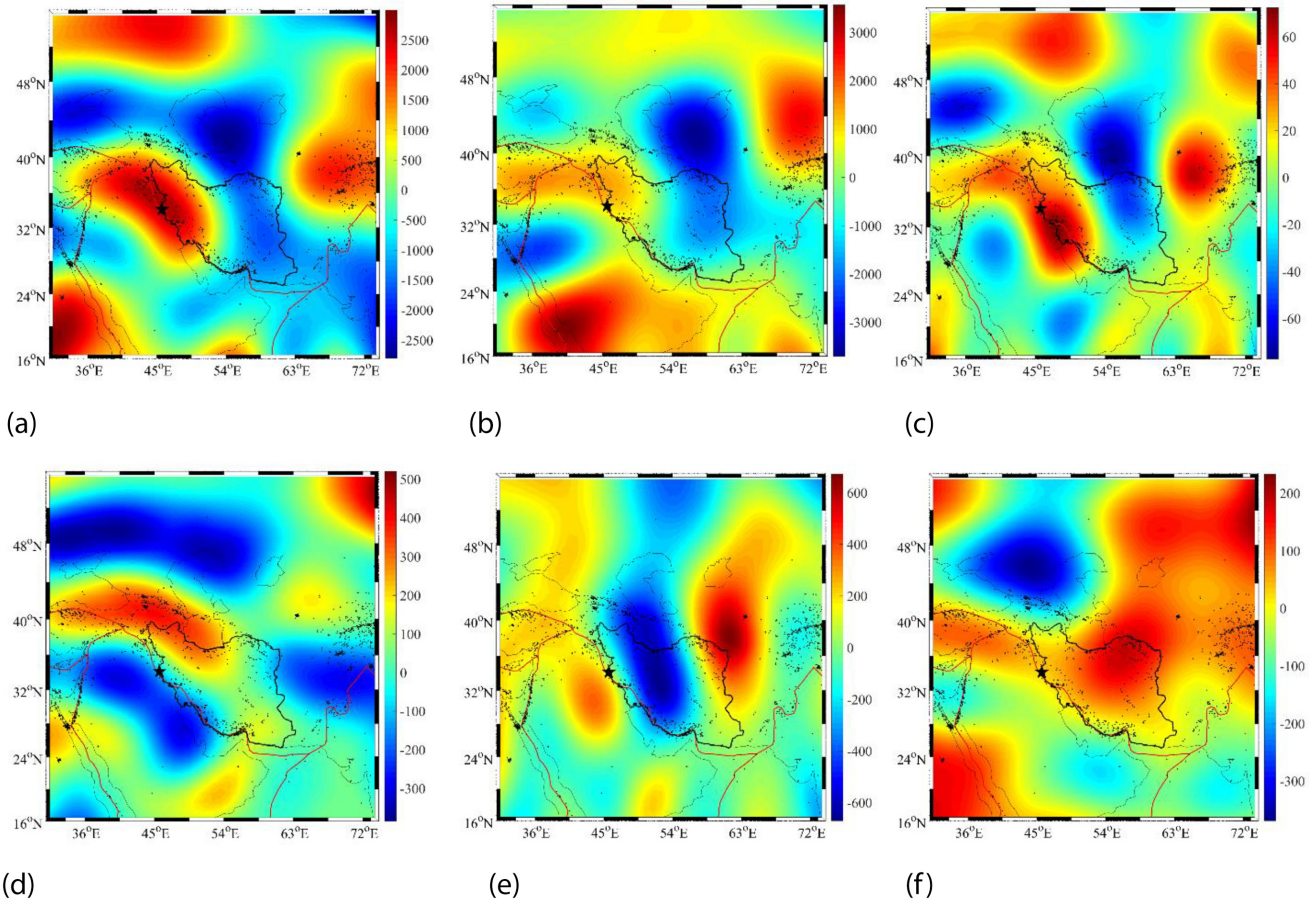

Figure 10. Changes in the stress tensor elements: (a) $\tau_{xx,}$ (b) $\tau_{yy,}$ (c) $\tau_{zz,}$ (d) $\tau_{xz,}$ (e) τ_{yz} and (f) τ_{xy} (Pa) between 2018 December and October computed from the GRACE-FO monthly solutions (from degree 10 to 30).

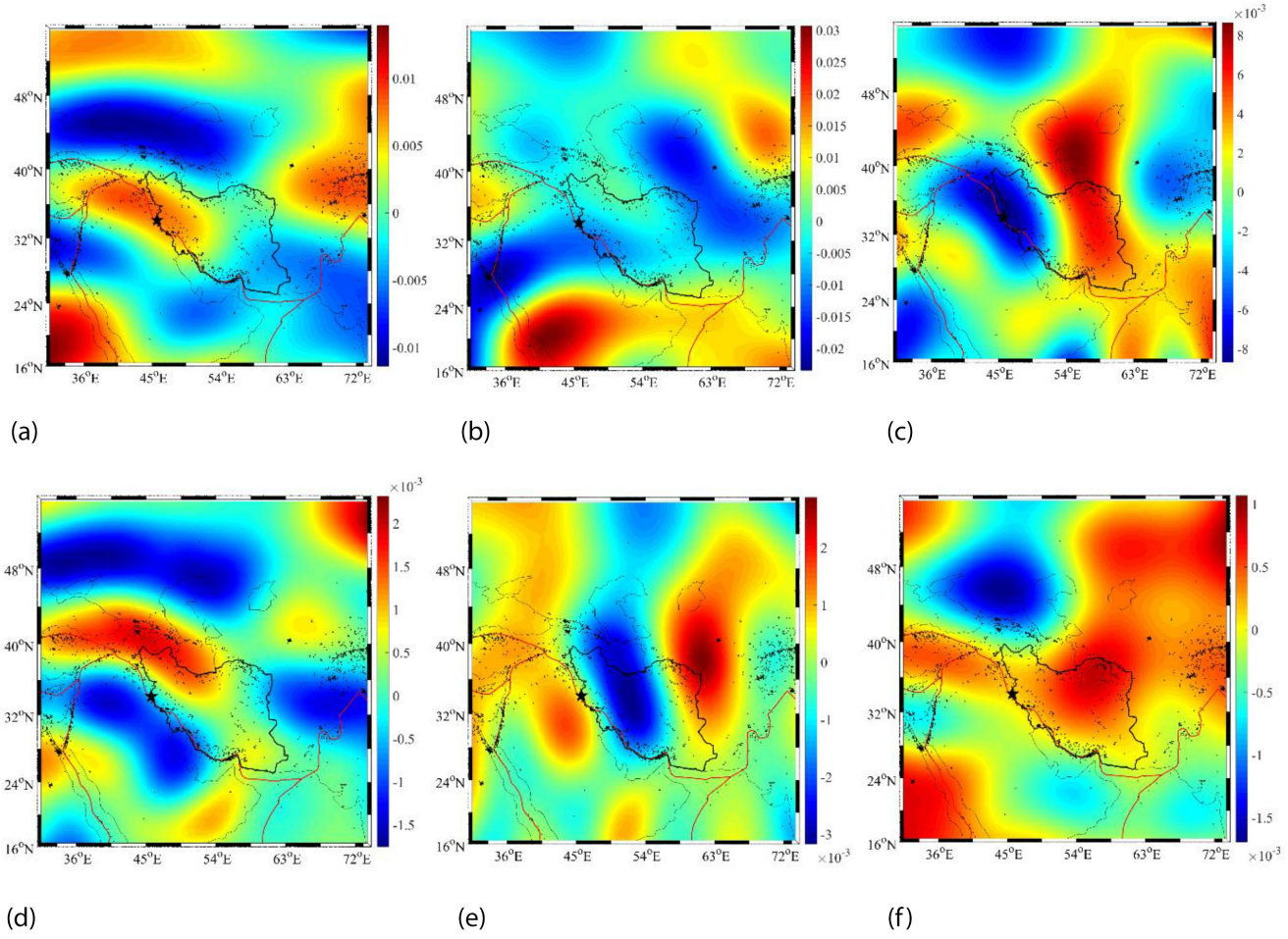

Figure 11. Changes in the strain tensor elements: (a) ε_{xx}, (b) ε_{yy}, (c) ε_{zz}, (d) ε_{xz}, (e) ε_{yz} and (f) ε_{xy} between 2018 December and October computed from the GRACE-FO monthly solutions.

4.6 Stress tensor changes

Changes in the stress tensor elements between 2018 December and October computed from the GRACE-FO monthly solutions (from degree 10 to 30) are shown in Fig. 10. In Fig. 10(a), we detected large changes in τ_{xx} in the vicinity of earthquake hypocentre, meaning that the earthquake pressed this area eastward. We also observed large changes of τ_{zz} in the vicinity of earthquake hypocentre, indicating an upward pressure (Fig. 10c). The corresponding changes in τ_{yy} are minor (Fig. 10b). A spatial pattern of changes in the normal stress tensor components (Figs 10a–c) indicate that the earthquake trigged a prevailing eastward and upward pressure that should also be recognized in the corresponding displacement changes (see Section 4.8). Changes in the shear stress components τ_{xz}, τ_{yz} and τ_{xy} are mainly manifested by their differences between the Arabian plate and the Iranian block (see Figs 10d–f).

4.7 Strain tensor changes

Changes in the strain tensor elements between 2018 December and October computed from the GRACE-FO monthly solutions are shown in Fig. 11. Comparing Figs 10 and 11, we could recognize that spatial patterns of changes in the stress and strain elements are generally similar. Some regional differences are more pronounced in the normal strain elements due to the fact that the volumetric strain was used to compute the normal stress elements according to eqs (5a)–(5c). Nevertheless, the earthquake caused quite large changes in the strain tensor elements ε_{xx} and ε_{zz} in the vicinity of earthquake hypocentre.

4.8 Displacement vector changes

The northward, eastward and upward displacement changes are visualized in Figs 12(a)–(c). Displacement changes due to the earthquake are relatively small, with maxima typically less than 1 mm. In agreement with large changes in the vertical normal stress τ_{zz} and strain ε_{zz} elements (Figs 10c and 11c), we detected relatively significant uplift in the vicinity of earthquake (Fig. 12c). A possible presence of eastward

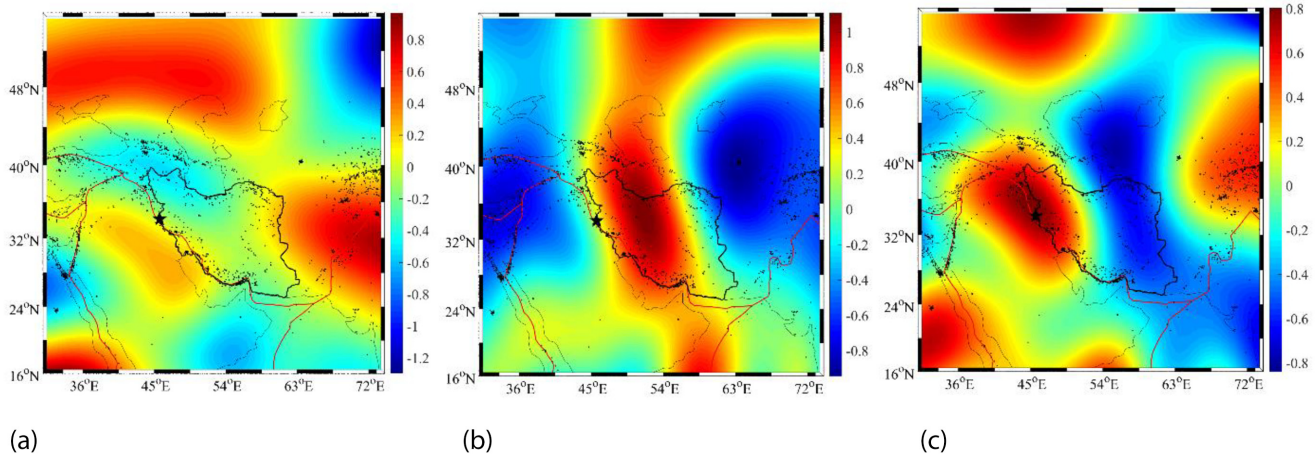

Figure 12. Changes in the displacement vector components: (a) s_x, (b) s_y and (c) s_z (mm) between 2018 December and October computed from the GRACE-FO monthly solutions (from degree 20 to 30).

motion is, on the other hand, not recognized. Instead, we see that the earthquake likely caused some horizontal divergence along the active tectonic margin between the Arabian plate and the Iranian block (Figs 12a and b).

5 SUMMARY AND CONCLUDING REMARKS

We have developed a theoretical model for inferring changes in the stress, strain and displacement fields from spatio-temporal gravity field variations. Functional relationships between changes in the stress, strain and displacements rates and gravity field variations were formulated based on solving the boundary-value problem of elasticity. The solution of this boundary-value problem requires adopting boundary conditions at the upper and lower boundary of the lithosphere approximated by a spherical shell. By analogy with Fu & Huang (1983), in our solution we assumed zero forces at the upper bound. We also assumed that the radial force is zero at the lower bound. By analogy with Runcorn's (1967) theory, we only assumed that the shear stress induced by a mantle convection flow is acting at LAB (approximated by a lower bound of lithospheric spherical shell). We then established the linear functional model for finding the coefficients A, B, C and D required to compute the displacement vector components (eqs 3g–3i), the strain tensor elements (eqs 4a–4f) and the stress tensor elements (eqs 5a–5f).

The solution to the boundary-value problem of elasticity for detecting changes in the stress, strain and displacement rates from spatio-temporal gravity variations required additional information about elastic parameters and thickness of the lithosphere. The depth of LAB was obtained from topographic and bathymetric data sets and a lithospheric thickness model. Elastic parameters of the lithosphere were derived from seismic velocities and mass densities within the lithosphere.

We applied developed theoretical models to detect changes in the stress, strain and displacement rates caused by the Sar-e-Pol Zahab earthquake that occurred on 2018 November 25 along active convergent tectonic margin between the Arabian plate and the Iranian block. For this purpose, we used the GRACE-FO monthly solutions corrected for the hydrological signal that was modelled from the GLDAS products.

Our results revealed that the earthquake caused changes in vertical displacement around its epicentre and divergent movements in the west–east direction and convergence in the north–south direction. Results also show that the earthquake mainly affected the normal stress elements τ_{xx} and τ_{zz} and the normal strain elements ε_{xx} and ε_{zz} in the proximity of the earthquake hypocentre, while corresponding changes in τ_{yy} and ε_{yy} were minor. We also find similarities in spatial patterns of changes between the shear stress and strain tensor elements. In general, spatial changes in the shear stress and strain rates relatively closely mimic active convergent tectonic margins, reflecting different displacements of the Arabian plate and the Iranian block caused by the earthquake.

ACKNOWLEDGEMENTS

The authors are thankful to Prof Michal Bevis at Ohio State University for proving the Matlab codes, for generating the mechanical parameters of the CRUST1.0 model. Robert Tenzer has been supported by the HK science project 1 ZE8F: remote-sensing data for studding Earth's and planetary inner structure.

REFERENCES

Alavi, M., 2004. Regional stratigraphy of the Zagros fold-thrust belt of Iran and its proforeland evolution, *Am. J. Sci.,* **304**(1), 1–20.

Berberian, M., 1976. Contribution to the seismotectonics of Iran (Part II), Geological Survey of Iran, Report No. 39, 141.

Bowin, C., 2000. Mass anomaly structure of the Earth, *Rev. Geophys.,* **38**(3), 355–387.

Chen, J.L., Wilson, C.R., Tapley, B.D. & Grand, S., 2007. GRACE detects coseismic and postseismic deformation from the Sumatra-Andaman earthquake. *Geophys. Res. Lett.,* **34**(13), L13302, doi.org/10.1029/2007GL030356

Chen, B., Kaban, M.K., El Khrepy, S. & Al-Arifi, N., 2015. Effective elastic thickness of the Arabian plate: weak shield versus strong platform. *Geophys. Res. Lett.,* **42**(9), 3298–3304.

Conrad, C.P. & Lithgow-Bertelloni, C., 2006. Influence of continental roots and asthenosphere on plate-mantle coupling, *Geophys. Res. Lett.,* **33**(5), L05312, doi.org/10.1029/2005GL025621.

Eshagh, M., 2014. From satellite gradiometry data to the sub-crustal stress due to the mantle convection, *Pure Appl. Geophys.,* **171,** 2391–2406.

Eshagh, M., 2015. On the relation between Moho and sub-crustal stress induced by mantle convection, *J. Geophys. Eng.,* **12,** 1–11.

Eshagh, M., 2017. Local recovery of lithospheric stress tensor from GOCE gravitational tensor, *Geophys. J. Int.,* **209,** 317–333.

Eshagh, M. & Romeshkani, M., 2015. Determination of sub-lithospheric stress due to mantle convection using GOCE gradiometric data over Iran. *J. appl. Geophys.,* **122,** 11–17.

Eshagh, M. & Tenzer, R., 2017. Lithospheric stress tensor from gravity and lithospheric structure models, *Pure Appl. Geophys.,* **174,** 2677–2688.

Eshagh, M., Hussain, M. & Tiampo, K.F., 2016. Towards sub-lithospheric stress determination from seismic Moho, topographic heights and GOCE data, *J. Asian Earth Sci.,* **169**(1), 1–12.

Eshagh, M., Steinberger, B., Tenzer, R. & Tassara, A., 2018. Comparison of gravimetric and mantle flow solutions for lithospheric stress modelling and their combination, *Geophys. J. Int.,* **213**(2), 1013–1028.

Eshagh, M., Tenzer, R. & Eshagh, M., 2019. Elastic thickness of the Iranian lithosphere from gravity and seismic data, *Tectonophysics,* **774,** 228186, doi.org/10.1016/j.tecto.2019.228186.

Farr, T.G. *et al.*, 2007. The Shuttle Radar Topography mission. *Rev. Geophys.,* **45**(2), doi.org/10.1029/2005RG000183.

Fatolazadeh, F., Raoofian Naeeni, M., Voosoghi, B. & Rahimi, A., 2017. Estimation of fault parameters using GRACE observations and analytical model. *J. Geodyn.,* **108,** 26–39.

Fu, R. & Huang, P., 1983. The global stress field in the lithosphere obtained from satellite gravitational harmonics, *Phys. Earth planet. Inter.,* **31**(3), 269–276.

Fu, R. & Huang, J., 1990. Global stress pattern constrained on deep mantle flow and tectonic features, *Phys. Earth Planet. Inter.,* **60**(1–4), 314–323.

Gu, Y.C., Yuan, L.G., Fan, D.M., You, W. & Su, Y., 2017. Seasonal crustal vertical deformation induced by environmental mass loading in mainland China derived from GPS, GRACE and surface loading models, *Adv. Space Res.,* **59**(1), 88–102.

Hager, B.H. & O'Connell, R.J., 1981. A simple global model of plate dynamics and mantle convection, *J. Geophys. Res.,* **86**(B6), 4843–4867.

He, M.L., Shen, W.B., Pan, Y., Chen, R., Ding, H. & Guo, G., 2018. Temporal–spatial surface seasonal mass changes and vertical crustal deformation in south China block from GPS and GRACE measurements, *Sensors,* **18**(1), 99, doi: 10.3390/s18010099.

Heidbach, O. *et al.*, 2018. The World Stress Map database release 2016: crustal stress pattern across scales. *Tectonophysics,* **744,** 484–498.

Jackson, J., Haines, J. & Holt, W., 1995. The accommodation of Arabia–Eurasia plate convergence in Iran, *J. Geophys. Res.,* **100**(BB), 15205–15219. doi.org/10.1029/95JB01294

Kaula, W.M., 1963. Elastic models of the mantle corresponding to variations in the external gravity field, *J. Geophys. Res.,* **68**(17), 4967–4978.

Kaviani, A., Hatzfeld, D., Paul, A., Tatar, M. & Priestley, K., 2009. Shear-wave splitting, ithospheric anisotropy and mantle deformation beneath the Arabia–Eurasia collision zone in Iran, *Earth Planet. Sci. Lett.,* **286**(3–4), 371–378.

Kornfeld, R.P., Arnold, B.W., Gross, M.A., Dahya, N.T., Klipstein, W.M., Gath, P.F. & Bettadpur, S., 2019. GRACE-FO: the gravity recovery and climate experiment follow-on mission, *J. Spacecr. Rockets,* **56**(3), doi.org/10.2514/1.A34326.

Laske, G., Masters, G., Ma, Z. & Pasyanos, M.E., 2013. Update on CRUST1.0—a 1-degree global model of Earth's crust. Geophysical Research Abstracts 15 (Abstract EGU2013-2658).

Liu, H.S., 1977. Convection pattern and stress system under the African plate, *Phys. Earth Planet. Inter.,* **15**(1), 60–68.

Liu, H.S., 1978. Mantle convection pattern and subcrustal stress under Asia, *Phys. Earth Planet. Inter.,* **16**(3), 247–256.

Liu, H.S., 1983. A dynamical basis for crustal deformation and seismotectonic block movements in central Europe, *Phys. Earth Planet. Inter.,* **32,** 146–159.

Li, S., Shen, W., Pan, Y. & Zhang, T., 2020. Surface seasonal mass changes and vertical crustal deformation in North China from GPS and GRACE measurements, *Geod. Geodyn.,* **11**(1), 46–55.

Love, A.E.H., 1944. *A Treatise on the Mathematical Theory of Elasticity,* Dover Publication, New York, p. 249.

Marsh, B.D. & Marsh, J.G., 1976. On global gravity anomalies and two-scale mantle convection, *J. Geophys. Res.,* **81**(29), 5267–5280.

McKenzie, D.P., 1967. Some remarks on heat flow and gravity anomalies, *J. Geophys. Res.,* **72**(24), 6261–6273.

McNutt, M., 1980. Implication of regional gravity for state of stress in the Earth's crust and upper mantle, *J. Geophys. Res.,* **85**(B11), 6377–6396.

Means, W.D., 1976. *Stress and Strain,* Springer, Heidelberg.

Medvedev, S., 2016. Understanding lithospheric stresses: systematic analysis of controlling mechanisms with applications to the African Plate, *Geophys. J. Int.,* **207,** 393–413.

Pan, Y., Shen, W.B., Hwang, C., Liao, C., Zhang, T. & Zhang, G., 2016. Seasonal mass changes and crustal vertical deformations constrained by GPS and GRACE in Northeastern Tibet, *Sensors,* **16**(8), 1211, doi: 10.3390/s16081211.

Phillips, R.J. & Ivins, E.R., 1979. Geophysical observations pertaining to solid-state convection in the terrestrial planets, *Phys. Earth Planet. Inter.,* **19**(2), 107–148.

Pollastro, R.M., Persits, F.M. & Steinshouer, D.W., 1997. Map showing Geology, Oil and Gas Fields, and Geologic Provinces of Iran, Report 97–470, The Survey: USGS Information Service, ISBN: 0607936908.

Rathnayake, S., Tenzer, R., Eshagh, M. & Pitoňák, M., 2019. Gravity maps of the lithospheric structure beneath the Indian Ocean, *Surv. Geophys.,* **40,** 1055–1093.

Ricard, Y., Fleitout, L. & Froidevaux, C., 1984. Geoid heights and lithospheric stresses for a dynamic Earth, *Ann. Geophys.,* **2**(3), 267–286.

Richards, M.A. & Hager, B.H., 1984. Geoid anomalies in a dynamic Earth, *J. Geophys. Res.,* **89**(B7), 5987–6002.

Rodell, M. *et al.*, 2004. The Global Land Data Assimilation System, *Bull. Am. Meteorol. Soc.,* **85,** 381–394.

Runcorn, S.K., 1964. Satellite gravity measurements and laminar viscous flow model of the Earth mantle, *J. Geophys. Res.,* **69**(20), 4389–4394.

Runcorn, S.K., 1967. Flow in the mantle inferred from the low degree harmonics of the geopotential, *Geophys. J. Int.,* **14**(1–4), 375–384.

Steinberger, B., Schmeling, H. & Marquart, G., 2001. Large-scale lithospheric stress field and topography induced by global mantle circulation, *Earth Planet. Sci. Lett.,* **186**(1), 75–91.

Stewart, J. & Watts, A.B., 1997. Gravity anomalies and spatial variations of flexural rigidity at mountain ranges, *J. Geophys. Res.,* **102**(B3), 5327–5352.

Stöcklin, J., 1968. Structural history and tectonics of Iran: a review, *Am. Assoc. Petrol. Geol. Bull.,* **52**(7), 1229–1258.

Stuewe, K., 2007. *Geodynamics of the Lithosphere,* 2nd ed., Berlin, Springer

Sun, W. & Okubo, S., 2004. Coseismic deformations detectable by satellite gravity missions—a case study of Alaska (1964, 2002) and Hokkaido (2003) earthquakes in the spectral domain, *J. Geophys. Res.,* **109**(B4), B04405, doi.org/10.1029/2003JB002554.

Tanaka, Y.S., Heki, K., Matsuo, K. & Shestakov, N.V., 2015. Crustal subsidence observed by GRACE after the 2013 Okhotsk deep-focus earthquake, *Geophys. Res. Lett.* **42**(9), 3204–3209.

Tapley, B. *et al.*, 2005. GGM02—an improved Earth gravity field model from GRACE, *J. Geod.,* **79,** 467–478.

Tenzer, R., Hamayun, K. & Vajda, P., 2009. Global maps of the CRUST2.0 components stripped gravity disturbances, *J. Geophys. Res. (Solid Earth),* **114**(B5), B05408, doi.org/10.1029/2008JB006016.

Tenzer, R., Gladkikh, V., Vajda, P. & Novák, P., 2012. Spatial and spectral analysis of refined gravity data for modelling the crust-mantle interface and mantle-lithosphere structure, *Surv. Geophys.,* **33**(5), 817–839.

Tenzer, R., Chen, W., Tsoulis, D., Bagherbandi, M., Sjöberg, L.E., Novák, P. & Jin, S., 2015. Analysis of the refined CRUST1.0 crustal model and its gravity field, *Surv. Geophys.,* **36**(1), 139–165.

Tesmer, V., Steigenberger, P., Van Dam, T. & Mayer-Gürr, T., 2011. Vertical deformations from homogeneously processed GRACE and global GPS long-term series, *J. Geod.,* **85,** 291–310.

Turcotte, D. & Schubert, G., 2014. *Geodynamics,* 3rd edn, Cambridge University Press.

Wahr, J., Molenaar, M. & Bryan, F., 1998. Time variability of the Earth's gravity field: hydrological and oceanic effects and their possible detection using GRACE, *J. Geophys. Res. (Solid Earth),* **103**(B12), 30205–30229.

Wang, L., Chen, C., Du, J. & Wang, T., 2017. Detecting seasonal and long-term vertical displacement in the North China Plain using GRACE and GPS, *Hydrol. Earth Syst. Sci.,* **21,** 2905–2922.

Wu, Y., Zhao, Q., Zhang, B. & Wu, W., 2017. Characterizing the seasonal crustal motion in Tianshan area using GPS, GRACE and Surface Loading Models, *Remote Sens.,* **9**(12), 1303, doi.org/10.3390/rs9121303.

Xu, C., Su, X., Liu, T. & Sun, W., 2017. Geodetic observations of the co- and post-seismic deformation of the 2013 Okhotsk Sea deep-focus earthquake, *Geophys. J. Int.,* **209**(3), 1924–1933.

Zamani, A. & Hashemi, N., 2000. A comparison between seismicity, topographic relief, and gravity anomalies of the Iranian Plateau, *Tectonophysics,* **327**(1–2), 25–36.

Zamani, A. & Hashemi, N., 2004. Computer-based self-organized tectonic zoning: a tentative pattern recognition for Iran, *Comput. Geosci.,* **30,** 7705–7718.

Zamani, A. & Agh-Atabai, M., 2009. Temporal characteristics of seismicity in the Alborz and Zagros regions of Iran, using a multifractal approach, *J. Geodyn.,* **47**(5), 271–279.

Zamani, B., Angelier, J. & Zamani, A., 2008. State of stress induced by plate convergence and stress partitioning in northeastern Iran, as indicated by focal mechanisms of earthquakes, *J. Geodyn.,* **45**(2–3), 120–132.

Zamani, A., Samiee, J. & Kirby, J.F., 2013. Estimating the mechanical anisotropy of the Iranian lithosphere using the wavelet coherence method, *Tectonophysics,* **601,** 139–147.

Zang, A. & Stephansson, O., 2010. *Stress Field of the Earth's Crust*. Springer, New York.

Zou, R., Wang, Q., Freymueller, J.T., Poutanen, M., Cao, X., Zhang, C., Yang, S. & He, P., 2015. Seasonal hydrological loading in southern Tibet detected by joint analysis of GPS and GRACE, *Sensors,* **15**(12), 30525–30538.